



Title	Electric field thermopower modulation analyses of the operation mechanism of transparent amorphous SnO <sub>2</sub> thin-film transistor
Author(s)	Liang, Dou-dou; Zhang, Yu-qiao; Cho, Hai Jun; Ohta, Hiromichi
Citation	Applied physics letters, 116(14), 143503 <a href="https://doi.org/10.1063/5.0003153">https://doi.org/10.1063/5.0003153</a>
Issue Date	2020-04-06
Doc URL	<a href="http://hdl.handle.net/2115/80828">http://hdl.handle.net/2115/80828</a>
Rights	This article may be downloaded for personal use only. Any other use requires prior permission of the author and AIP Publishing. This article appeared in Liang Dou-dou, Zhang Yu-qiao, Cho Hai Jun, Ohta Hiromichi. Electric field thermopower modulation analyses of the operation mechanism of transparent amorphous SnO <sub>2</sub> thin-film transistor. Applied physics letters, 116, 143503 (2020) and may be found at <a href="https://doi.org/10.1063/5.0003153">https://doi.org/10.1063/5.0003153</a> .
Type	article
File Information	5.0003153.pdf



[Instructions for use](#)

# Electric field thermopower modulation analyses of the operation mechanism of transparent amorphous SnO<sub>2</sub> thin-film transistor

Cite as: Appl. Phys. Lett. **116**, 143503 (2020); <https://doi.org/10.1063/5.0003153>

Submitted: 30 January 2020 . Accepted: 22 March 2020 . Published Online: 07 April 2020

Dou-dou Liang , Yu-qiao Zhang , Hai Jun Cho , and Hiromichi Ohta 



View Online



Export Citation



CrossMark

## ARTICLES YOU MAY BE INTERESTED IN

[Solution-processed ITO thin-film transistors with doping of gallium oxide show high on-off ratios and work at 1 mV drain voltage](#)

Applied Physics Letters **116**, 141604 (2020); <https://doi.org/10.1063/1.5141140>

[Scaling-down and interfacial effect to break down the trade-off between thermal stability and crystallization speed of the Sb<sub>2</sub>Se films](#)

Applied Physics Letters **116**, 141601 (2020); <https://doi.org/10.1063/1.5143060>

[High electrical conducting deep-ultraviolet-transparent oxide semiconductor La-doped SrSnO<sub>3</sub> exceeding  \$\sim 3000 \text{ S cm}^{-1}\$](#)

Applied Physics Letters **116**, 022103 (2020); <https://doi.org/10.1063/1.5128410>

Lock-in Amplifiers  
up to 600 MHz



Watch



# Electric field thermopower modulation analyses of the operation mechanism of transparent amorphous SnO<sub>2</sub> thin-film transistor

Cite as: Appl. Phys. Lett. **116**, 143503 (2020); doi: 10.1063/5.0003153

Submitted: 30 January 2020 · Accepted: 22 March 2020 ·

Published Online: 7 April 2020



View Online



Export Citation



CrossMark

Dou-dou Liang,<sup>1,2,a)</sup> Yu-qiao Zhang,<sup>2</sup> Hai Jun Cho,<sup>2</sup> and Hiromichi Ohta<sup>2,a)</sup>

## AFFILIATIONS

<sup>1</sup>The Beijing Municipal Key Laboratory of New Energy Materials and Technologies, School of Materials Science and Engineering, University of Science and Technology Beijing, Beijing 100083, China

<sup>2</sup>Research Institute for Electronic Science, Hokkaido University, N20W10, Kita, Sapporo 001-0020, Japan

<sup>a)</sup>Authors to whom correspondence should be addressed: liangdoudou1993@foxmail.com and hiromichi.ohta@es.hokudai.ac.jp

## ABSTRACT

Transparent amorphous oxide semiconductors (TAOSs) based transparent thin-film transistors (TTFTs) with high field effect mobility ( $\mu_{FE}$ ) are essential for developing advanced flat panel displays. Among TAOSs, amorphous (a-) SnO<sub>2</sub> has several advantages against current a-InGaZnO<sub>4</sub> such as higher  $\mu_{FE}$  and being indium-free. Although a-SnO<sub>2</sub> TTFT has been demonstrated several times, the operation mechanism has not been clarified thus far due to the strong gas sensing characteristics of SnO<sub>2</sub>. Here we clarify the operation mechanism of a-SnO<sub>2</sub> TTFT by electric field thermopower modulation analyses. We prepared a bottom-gate top-contact type TTFT using 4.2-nm-thick a-SnO<sub>2</sub> as the channel without any surface passivation. The effective thickness of the conducting channel was  $\sim 1.7 \pm 0.4$  nm in air and in vacuum, but a large threshold gate voltage shift occurred in different atmospheres; this is attributed to carrier depletion near at the top surface ( $\sim 2.5$  nm) of the a-SnO<sub>2</sub> due to its interaction with the gas molecules and the resulting shift in the Fermi energy. The present results would provide a fundamental design concept to develop a-SnO<sub>2</sub> TTFT.

Published under license by AIP Publishing. <https://doi.org/10.1063/5.0003153>

Transparent amorphous oxide semiconductors (TAOSs) based transparent thin-film transistors (TTFTs) with high field effect mobility ( $\mu_{FE}$ ) are essential components for advanced flat panel displays such as transparent organic light-emitting diode (OLED) displays and rollable OLED displays. Currently, amorphous (a-) InGaZnO<sub>4</sub> is widely applied as the TAOS<sup>1-4</sup> of the TFT channel of commercially available OLED displays; the optical bandgap of a-InGaZnO<sub>4</sub> is  $\sim 3$  eV,<sup>5</sup> transparent in the visible light region, and the  $\mu_{FE}$  of a-InGaZnO<sub>4</sub> ( $\sim 10$  cm<sup>2</sup> V<sup>-1</sup> s<sup>-11,2</sup>) is two orders of magnitude higher than that of previously used a-Si. However, the use of a-InGaZnO<sub>4</sub> must be reduced because the consumption of rare element such as indium (Clarke number:  $1 \times 10^{-5}\%$ ) is not desirable for maintaining sustainable usage of resources. Therefore, development of post-a-InGaZnO<sub>4</sub> TAOSs showing high  $\mu_{FE}$ , which are composed of abundant elements, is crucial.

Among several indium-free TAOSs,<sup>6-8</sup> a-SnO<sub>2</sub> is a promising candidate for overcoming the issues with a-InGaZnO<sub>4</sub>. Sn is one of the abundant metal elements with the Clarke number<sup>9</sup> of Sn which is  $4 \times 10^{-3}\%$ , 400 times larger than that of In. Moreover, SnO<sub>2</sub> TFT shows

extremely high  $\mu_{FE} > 100$  cm<sup>2</sup> V<sup>-1</sup> s<sup>-1,10-12</sup> which is one order of magnitude higher than that of a-InGaZnO<sub>4</sub>. In 2007, Dattoli *et al.*<sup>10</sup> reported that Ta-doped SnO<sub>2</sub> nanowire TFT exhibits uniform characteristics with average  $\mu_{FE}$  exceeding 100 cm<sup>2</sup> V<sup>-1</sup> s<sup>-1</sup> at room temperature. In 2009, Sun *et al.*<sup>11</sup> fabricated Sb-doped SnO<sub>2</sub> nanocrystal TFTs at room temperature with  $\mu_{FE}$  of 158 cm<sup>2</sup> V<sup>-1</sup> s<sup>-1</sup>. In 2016, Shin *et al.*<sup>12</sup> reported that an extremely thin ( $< 4.5$  nm) undoped SnO<sub>2</sub> TFT exhibited  $\mu_{FE}$  of 150 cm<sup>2</sup> V<sup>-1</sup> s<sup>-1</sup> at room temperature in air. In these reports, bottom-gate top-contact type TFTs without any passivation showed high  $\mu_{FE}$ . Thus, the top surface of SnO<sub>2</sub> channel was exposed to the atmosphere.

SnO<sub>2</sub> is a well-known gas sensing material.<sup>13,14</sup> It is known that a 3–4-nm-thick depletion layer is formed at the SnO<sub>2</sub> surface.<sup>15,16</sup> Oxygen molecules in the ambient atmosphere are adsorbed on the surface, seize free electrons near the surface, and form a depletion layer. In a reducing atmosphere, parts of the seized electrons are released back to the depletion layer. Thus, the transistor characteristics of the bottom-gate top-contact type SnO<sub>2</sub> TFTs would be strongly affected by the gases surrounding the exposed channel surface due to their gas sensing property. For this reason, the operation mechanism of the bottom-gate

top-contact type SnO<sub>2</sub> TFTs including the conduction band bending and the effective channel thickness have not been clarified thus far.

Here we clarify the conduction band bending and the effective channel thickness of 4.2-nm-thick a-SnO<sub>2</sub> based bottom-gate top-contact type TTFTs without any surface passivation. We analyzed the conduction band bending of the SnO<sub>2</sub> top surface by measuring the TFT characteristics in air and vacuum, and a large threshold gate voltage shift was observed; the Fermi energy in the carrier depletion region at the top surface (~2.5 nm) of the a-SnO<sub>2</sub> channel sensitively shifted with the changes in the gas atmosphere. The effective channel thickness ( $t_{\text{eff}}$ ) was analyzed by the electric field thermopower (S) modulation method,<sup>17–21</sup> and the  $t_{\text{eff}}$  was  $\sim 1.7 \pm 0.4$  nm in air and in vacuum. The present results would provide a fundamental design concept for developing a-SnO<sub>2</sub> TTFT.

The bottom-gate top-contact TTFTs (Fig. 1) were fabricated on 100-nm-thick ITO coated alkali-free glass (thickness: 0.7 mm, Corning® EAGLE XG®) substrates by pulsed laser deposition (PLD, KrF excimer laser, 10 Hz) technique. First, a 300-nm-thick polycrystalline Y<sub>2</sub>O<sub>3</sub> gate dielectric film (the dielectric permittivity,  $\epsilon_r = 20$ <sup>22</sup>) was deposited at room temperature. The fluence of the KrF laser was  $\sim 2$  J cm<sup>-2</sup> pulse<sup>-1</sup>, and the oxygen pressure was kept at 0.4 Pa during deposition. Then, a 4.2-nm-thick SnO<sub>2</sub> film was deposited on the Y<sub>2</sub>O<sub>3</sub>/ITO bilayer laminate through a stencil mask at 300 °C [see supplementary material Figs. S1(a) and S1(b)]. The fluence of the KrF laser was  $\sim 0.3$  J cm<sup>-2</sup> pulse<sup>-1</sup>, and the oxygen pressure was kept at 1 Pa during the deposition. The optical bandgap ( $E_g$ ) of the a-SnO<sub>2</sub> film was  $\sim 4.3$  eV [supplementary material Fig. S1(c)], which was larger than that of bulk SnO<sub>2</sub> ( $E_g \sim 3.6$  eV).<sup>23</sup> This is most likely due to the quantum size effect.<sup>24</sup> Finally, 100-nm-thick ITO films, which were used as the source and drain electrodes (400  $\mu\text{m} \times 400 \mu\text{m}$ ), were deposited at room temperature. The fluence of the KrF laser was  $\sim 0.9$  J cm<sup>-2</sup> pulse<sup>-1</sup> and the oxygen pressure was kept at 3 Pa during deposition. After these PLD processes, the device was annealed at 400 °C for 30 min in air. The channel length  $L$  and the channel width

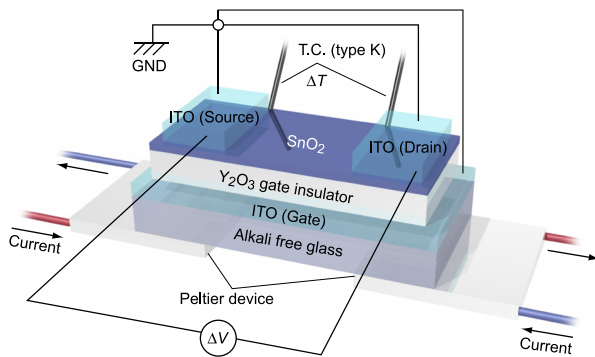


**FIG. 1.** Electric field thermopower modulation measurement of the bottom-gate top-contact a-SnO<sub>2</sub> TTFT. The top surface of the 4.2-nm-thick SnO<sub>2</sub> channel is exposed to the air. The channel length  $L$  is 200  $\mu\text{m}$  and the channel width  $W$  is 400  $\mu\text{m}$ . The gate insulator is 300-nm-thick polycrystalline Y<sub>2</sub>O<sub>3</sub> ( $\epsilon_r = 20$ ). The SnO<sub>2</sub> channel is placed on the gap ( $\sim 2$  mm) between two Peltier devices, which are used to give temperature difference ( $\Delta T$ ) between both edges of the channel. Two K-type thermocouples (T.C.) are located at both edges of the SnO<sub>2</sub> channel to measure the temperature difference between both edges of the SnO<sub>2</sub> channel. The thermoelectromotive force ( $\Delta V$ ) and  $\Delta T$  are measured simultaneously at a fixed gate voltage ( $V_g$ ).

$W$  of the resultant TFT were 200 and 400  $\mu\text{m}$ , respectively. The resultant multiple layer was fully transparent in the visible light region (supplementary material Fig. S2).

The TTFT characteristics such as transfer characteristics ( $I_d$ - $V_g$ ) and output characteristics ( $I_d$ - $V_d$ ) were measured using a semiconductor device analyzer (B1500A, Agilent Co.) at room temperature. As shown in Fig. 2(a), the resultant TTFTs showed clear transfer ( $I_d$ - $V_g$ ) characteristics with the on-to-off current ratios of  $\sim 10^5$ . All the TFTs show clear pinch-off in the output characteristics [supplementary material Fig. S3], indicating that the TTFT operation obeys the standard field-effect theory. It should be noted that the threshold gate voltage ( $V_{\text{th}}$ ), which was evaluated by plotting  $I_d^{0.5}$ - $V_g$  relationship, was  $-14$  V in air but shifted dramatically to  $-23$  V in vacuum. The  $\mu_{\text{FE}}$ , calculated from  $\mu_{\text{FE}} = g_m \cdot [(W/L) \cdot C_i \cdot V_{\text{d}}]^{-1}$ , where  $g_m$  is the transconductance  $\partial I_d / \partial V_g$  and  $C_i$  is capacitance per unit area ( $C_i \sim 58$  nF cm<sup>-2</sup>),<sup>22</sup> was  $\sim 20$  cm<sup>2</sup> V<sup>-1</sup> s<sup>-1</sup> in air and  $\sim 30$  cm<sup>2</sup> V<sup>-1</sup> s<sup>-1</sup> in vacuum. These confirm that the channel conductance and the  $V_{\text{th}}$  indeed can be modulated with the gases surrounding exposed a-SnO<sub>2</sub> channel. The SnO<sub>2</sub> TTFT characteristics were summarized in Table I.

The electric field modulated thermopower (S) was measured during the transfer characteristics measurements in the two gas

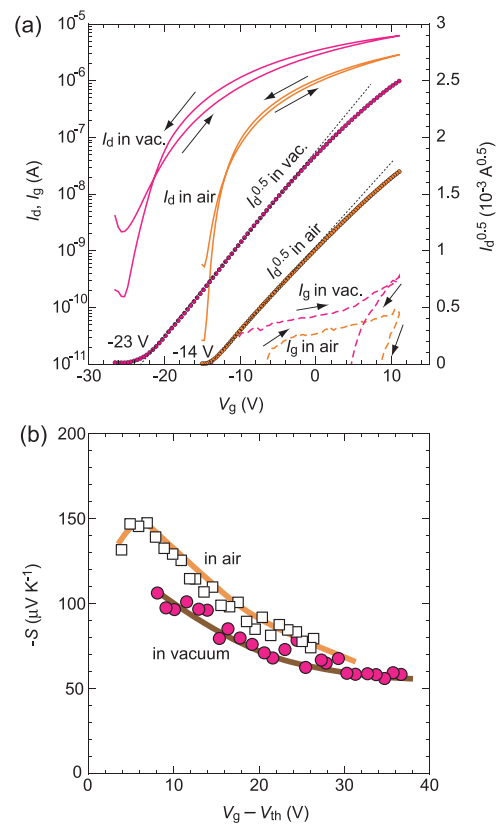


**FIG. 2.** Transistor characteristics the bottom-gate top-contact a-SnO<sub>2</sub> TTFT measured in air and in vacuum. (a) Transfer characteristic ( $I_d$ - $V_g$ ) curve at  $V_d = +0.1$  V. Corresponding  $I_d^{0.5}$ - $V_g$  and  $I_g$ - $V_g$  curves are also shown. The threshold voltage ( $V_{\text{th}}$ ) is  $-14$  V in air and  $-23$  V in vacuum. The gate leakage current ( $I_g$ ) is  $< 100$  pA. (b) Electric field modulated thermopower (S) at various  $V_g - V_{\text{th}}$  ranging from  $+4$  V to  $+37$  V. The  $-S$  gradually decreases with  $V_g - V_{\text{th}}$ .

**TABLE I.** On-f current ratio, threshold gate voltage ( $V_{th}$ ), subthreshold swing factor (S.S.), and field effect mobility ( $\mu_{FE}$ ) for SnO<sub>2</sub> TTFT.

	ON/OFF	$V_{th}$ (V)	S.S. (V decade <sup>-1</sup> )	$\mu_{FE}^{max}$ (cm <sup>2</sup> V <sup>-1</sup> s <sup>-1</sup> )
Air	$\sim 10^5$	-14	$0.65 \pm 0.02$	20
Vacuum	$\sim 10^5$	-23	$1.57 \pm 0.2$	30

atmospheres (air, vacuum) to analyze the  $t_{eff}$ . Details of the electric field modulated  $S$  measurement are described elsewhere.<sup>17–20</sup> Figure 2(b) shows the changes in  $-S$  as a function of the effective gate voltage ( $V_g - V_{th}$ ). The  $S$  values were always negative, consistent with the fact that the SnO<sub>2</sub> film is  $n$ -type semiconductor. The absolute values of  $S$  decrease gradually with increasing  $V_g - V_{th}$  in both atmospheres due to an increase in the sheet carrier concentration ( $n_s$ ), which was deduced from  $n_s = C_i \cdot (V_g - V_{th}) \cdot e^{-1}$ . Although a small variation in  $S$  was observed due to the gate leakage current ( $I_{gl}$ ), the observed  $S$  could be used to analyze the  $t_{eff}$  since the variation is less than 10%, and the difference in the air and vacuum atmospheres is noticeably clear.

In order to extract the  $t_{eff}$ , we plotted  $-S$  as a function of  $n_s$  [Fig. 3(a)]. An almost linear relationship with a slope of  $\sim 120 \mu V K^{-1}$  decade<sup>-1</sup> was observed in the  $-S$  vs  $\log n_s$  plot when  $n_s$  exceeded  $2.5 \times 10^{12} \text{ cm}^{-2}$  in air, and a slope of  $\sim 84 \mu V K^{-1}$  decade<sup>-1</sup> was observed in the same plot when  $n_s$  exceeded  $2.9 \times 10^{12} \text{ cm}^{-2}$  in vacuum. We also plotted the three-dimensional carrier concentration ( $n_{3D}$ ) dependence of  $-S$  measured from separately prepared SnO<sub>2</sub> thin films [Fig. 3(b), Table S1]. From the  $-S$  vs  $\log n_{3D}$  relationship, the carrier effective mass ( $m^*$ ) of the SnO<sub>2</sub> films was extracted to be  $0.47 m_0$  using the following equations:

$$s = \frac{k_B}{e} \left( \frac{\left(r + \frac{5}{2}\right) F_{\left(r + \frac{3}{2}\right)}(\eta)}{\left(r + \frac{3}{2}\right) F_{\left(r + \frac{1}{2}\right)}(\eta)} - \eta \right), \quad (1)$$

$$n_{HI} = \frac{1}{eR_H} = \frac{8\pi(2m_d^*k_B T)^{\frac{3}{2}} \left(r + \frac{3}{2}\right)^2 F_{\left(r + \frac{1}{2}\right)}^2(\eta)}{\left(2r + \frac{3}{2}\right) F_{\left(2r + \frac{1}{2}\right)}(\eta)}, \quad (2)$$

$$F_n(\eta) = \int_0^\infty \frac{x^n}{1 + e^{x-\eta}} dx, \quad (3)$$

where  $F_n(\eta)$  is the  $n$ th order Fermi integral,  $\eta$  is the reduced fermi energy,  $r$  is the scattering factor,  $h$  is the Planck constant, and  $k_B$  is the Boltzmann constant. Because acoustic phonon scattering is commonly the main scattering mechanism for this material, the scattering factor  $r$  could be considered as  $-1/2$ .  $S$  only depends on the slope of the electronic density of states at the Fermi level, which depends on  $n_{3D}$ . Since the  $n_s$  measured from the transistor characteristics represents the projected  $n_{3D}$  within the  $t_{eff}$ , we can directly compare the  $-S$  vs  $\log n_s$  relationship with the  $-S$  vs  $\log n_{3D}$  relationship. The slope of  $-S$  vs  $\log n_{3D}$  plot [Fig. 3(b)] is comparable to that of the  $-S$  vs  $\log n_s$  plot [Fig. 3(a)], indicating that the  $E-k$  relation at the bottom of the conduction band is parabolic, and  $t_{eff}$  can be extracted as  $n_s/n_{3D}$ .

Several  $S$ -values around the lower  $n_s$  did not follow the straight line, probably due to that the non-parabolic shaped tail states just

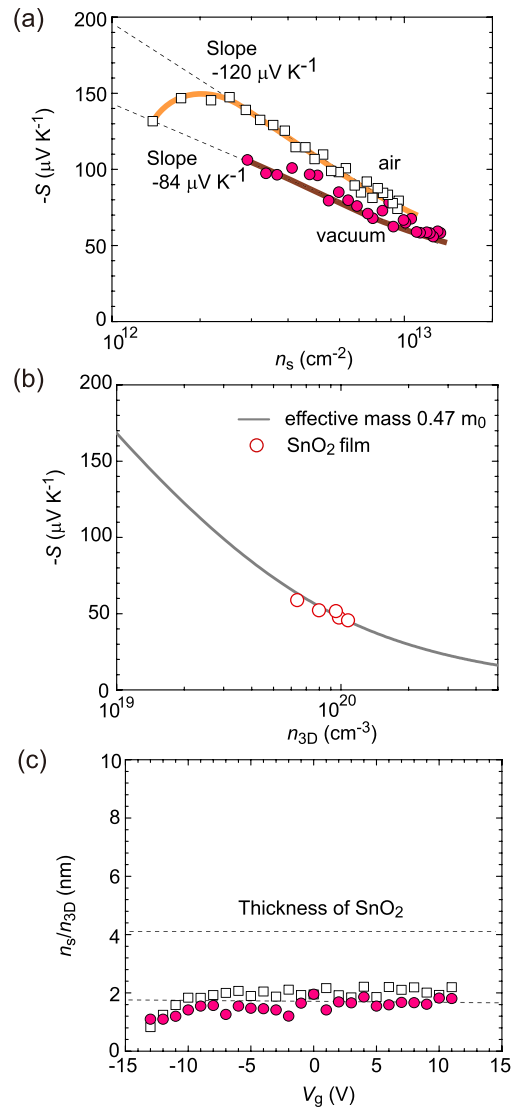


**FIG. 3.** Electric field thermopower modulation analyses of the bottom-gate top-contact a-SnO<sub>2</sub> TTFT. (a) Change in  $-S$  as a function of the sheet carrier concentration ( $n_s$ ). The slope of the  $-S-n_s$  relationship is  $-120 \mu V K^{-1}$  decade<sup>-1</sup> in air and  $-84 \mu V K^{-1}$  decade<sup>-1</sup> in vacuum (dotted line). (b) Three-dimensional carrier concentration ( $n_{3D}$ ) dependence  $S$  of the SnO<sub>2</sub> films. We calculated the carrier effective mass ( $m^*$ ) of the SnO<sub>2</sub> film around  $0.47 m_0$ . (c) The effective thickness ( $t_{eff}$ ), which is defined as  $n_s/n_{3D}$ , as a function of  $V_g$ . The  $t_{eff}$  is always  $\sim 1.7 \pm 0.4$  nm, insensitive to the atmosphere.

below the original conduction band bottom.<sup>18,22,25</sup> The  $S$  and  $n_s$  were modulated from  $(-150 \mu V K^{-1}, 2 \times 10^{12} \text{ cm}^{-2})$  to  $(-80 \mu V K^{-1}, 1 \times 10^{13} \text{ cm}^{-2})$  in air and from  $(-110 \mu V K^{-1}, 2.9 \times 10^{12} \text{ cm}^{-2})$  to  $(-60 \mu V K^{-1}, 1.3 \times 10^{13} \text{ cm}^{-2})$  in vacuum with increasing positive electric field in the a-SnO<sub>2</sub> channel. The difference between the measurements in air and in vacuum is attributed to the gas sensing property of SnO<sub>2</sub>, where O<sub>2</sub> molecules are adsorbed in air and released in vacuum. The  $t_{eff} \equiv n_s/n_{3D}$  of the conducting a-SnO<sub>2</sub> channel were always  $\sim 1.7 \pm 0.4$  nm, insensitive to the gas atmosphere [Fig. 3(c)].

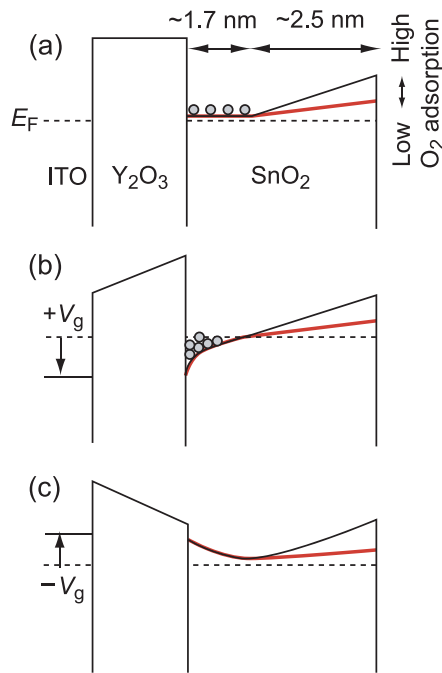


**FIG. 4.** Electric field modulation mechanism of the bottom-gate top-contact a-SnO<sub>2</sub> TTFT. (a) Without any gate voltage ( $V_g$ ) application. Conduction band minimum (CBM) around the surface is lifted due to oxygen gas adsorption. Black: higher oxygen atmosphere (air). Red: lower oxygen atmosphere (vacuum). The 2.5-nm-thick surface region is the surface depletion layer. The conducting channel ( $\sim 1.7$  nm) remains at the Y<sub>2</sub>O<sub>3</sub>/a-SnO<sub>2</sub> interface. The sheet carrier concentration ( $n_s$ ) is  $\sim 4 \times 10^{12}$  cm<sup>-2</sup>. (b) Under positive  $V_g$  application. The 1.7-nm-thick 2DEG layer is formed at the Y<sub>2</sub>O<sub>3</sub>/a-SnO<sub>2</sub> interface. The  $n_s$  increases up to  $\sim 1 \times 10^{13}$  cm<sup>-2</sup>. The surface region does not change. (c) Under negative  $V_g$  application, the interface electrons are completely depleted, resulting in off states.

Here, we would like to discuss the operation mechanism of a-SnO<sub>2</sub> TTFT [Fig. 4]. Without any  $V_g$  application [Fig. 4(a)], the conduction band minimum (CBM) at the surface is lifted due to the adsorption of oxygen when the TTFT is exposed to air (higher oxygen atmosphere, black line). When the TTFT is exposed to vacuum, the CBM at the surface is lowered (lower oxygen atmosphere, red line). Due to the oxygen adsorption, a 2.5-nm-thick depletion layer, which is similar to the Debye length of SnO<sub>2</sub> ( $\sim 3$  nm),<sup>26</sup> is formed near the surface region. As a result, a conducting channel ( $\sim 1.7 \pm 0.4$  nm) remains at the Y<sub>2</sub>O<sub>3</sub>/a-SnO<sub>2</sub> interface, and the  $n_s$  is  $\sim 4 \times 10^{12}$  cm<sup>-2</sup> ( $n_{3D} \sim 2 \times 10^{19}$  cm<sup>-3</sup>). Under positive  $V_g$  application [Fig. 4(b)], the carriers accumulate at the Y<sub>2</sub>O<sub>3</sub>/a-SnO<sub>2</sub> interface, and the  $E_F$  locates above the CBM. As a result, the 1.7-nm-thick 2D electron gas (2DEG) is formed at the Y<sub>2</sub>O<sub>3</sub>/a-SnO<sub>2</sub> interface. The  $n_s$  increases up to  $\sim 1 \times 10^{13}$  cm<sup>-2</sup> ( $n_{3D} \sim 4 \times 10^{19}$  cm<sup>-3</sup>). The surface region does not change. Under negative  $V_g$  application [Fig. 4(c)], the conduction electrons at the Y<sub>2</sub>O<sub>3</sub>/a-SnO<sub>2</sub> interface are completely depleted, showing off states in the transistor characteristics.

In summary, we have clarified the operation mechanism including the conduction band bending and the effective channel thickness ( $t_{\text{eff}}$ ) of 4.2-nm-thick a-SnO<sub>2</sub> based bottom-gate top-contact type TTFTs without any surface passivation. We analyzed the conduction band bending of SnO<sub>2</sub> top surface by measuring the TFT

characteristics in air as well as in vacuum and found the large threshold gate voltage shift; the Fermi energy in the carrier depletion region at the top surface ( $\sim 2.5$  nm) of the a-SnO<sub>2</sub> sensitively shifted depending on the gas atmospheres. We also analyzed the  $t_{\text{eff}}$  ( $\equiv n_s/n_{3D}$ ) by the electric field thermopower modulation method.  $t_{\text{eff}}$  was  $\sim 1.7 \pm 0.4$  nm in air and in vacuum.

From the thickness of the a-SnO<sub>2</sub> film (4.2 nm) and the  $t_{\text{eff}}$  ( $1.7 \pm 0.4$  nm), the carrier depletion depth at the top surface of the a-SnO<sub>2</sub> film is estimated to be 2.5 nm, which is similar to the depletion length reported in other studies.<sup>15,16</sup> When a-SnO<sub>2</sub> bottom-gate top-contact TTFTs are exposed to air, oxygen gas would be adsorbed on the surface of SnO<sub>2</sub> film as electron accepting species, which is accompanied by the formation of a depletion layer inside the film. The present results may provide a fundamental design concept for utilizing a-SnO<sub>2</sub> TFT in device applications.

See the [supplementary material](#) for additional crystallographic analyses of the SnO<sub>2</sub> thin film, optical transmission of the bottom-gate top-contact a-SnO<sub>2</sub> TTFT, transistor characteristics of the bottom-gate top-contact a-SnO<sub>2</sub> TTFT, and optical absorption spectrum of the polycrystalline Y<sub>2</sub>O<sub>3</sub> thin film deposited on the SiO<sub>2</sub> glass substrate.

This research was supported by Grants-in-Aid for Innovative Areas (No. 19H05791) and Scientific Research A (No. 17H01314) from the JSPS. D.L. greatly appreciates the support from China Scholarships Council (No. 201806460051). Y.Z. acknowledges the support from Grant-in-Aid for JSPS Fellows (No. 19F1904909) from the JSPS. H.J.C. acknowledges the support from Nippon Sheet Glass Foundation for Materials Science and Engineering. H.O. acknowledges the support from the Asahi Glass Foundation and the Mitsubishi Foundation. A part of this work was also supported by Dynamic Alliance for Open Innovation Bridging Human, Environment, and Materials, and by the Network Joint Research Center for Materials and Devices.

## REFERENCES

- K. Nomura, H. Ohta, A. Takagi, T. Kamiya, M. Hirano, and H. Hosono, *Nature* **432**, 488 (2004).
- K. Nomura, A. Takagi, T. Kamiya, H. Ohta, M. Hirano, and H. Hosono, *Jpn. J. Appl. Phys., Part 1* **45**, 4303 (2006).
- T. Kamiya and H. Hosono, *Npg Asia Mater.* **2**, 15 (2010).
- H. Hosono, *Nat. Electron.* **1**, 428 (2018).
- M. Orita, H. Ohta, M. Hirano, S. Narushima, and H. Hosono, *Philos. Mag. B* **81**, 501 (2001).
- P. Gorrn, M. Sander, J. Meyer, M. Kroger, E. Becker, H. H. Johannes, W. Kowalsky, and T. Riedl, *Adv. Mater.* **18**, 738 (2006).
- D. Jousse, C. Constantino, and I. Chambouleyron, *J. Appl. Phys.* **54**, 431 (1983).
- S. H. Sim, K. T. Kang, S. Lee, M. Lee, H. Taniguchi, S. Kim, S. Roh, J. H. Oh, S. A. Lee, J.-S. Bae, J. H. Jang, J. Hwang, S. Han, T. Park, and W. S. Choi, *Chem. Mater.* **31**, 8019 (2019).
- F. W. Clarke and H. S. Washington, *The Composition of the Earth's Crust* (U.S. Government Printing Office, 1924).
- E. N. Dattoli, Q. Wan, W. Guo, Y. B. Chen, X. Q. Pan, and W. Lu, *Nano Lett.* **7**, 2463 (2007).
- J. Sun, A. X. Lu, L. P. Wang, Y. Hu, and Q. Wan, *Nanotechnology* **20**, 335204 (2009).
- C. W. Shin, A. Chin, C. F. Lu, and W. F. Su, *Sci. Rep.* **6**, 19023 (2016).
- D. H. Kim, W. S. Kim, S. B. Lee, and S. H. Hong, *Sens. Actuators, B* **147**, 653 (2010).
- S. Das and V. Jayaraman, *Prog. Mater. Sci.* **66**, 112 (2014).
- N. Yamazoe, *Sens. Actuators, B* **5**, 7 (1991).
- V. Lantto, T. T. Rantala, and T. S. Rantala, *J. Eur. Ceram. Soc.* **21**, 1961 (2001).

- <sup>17</sup>A. V. Sanchela, M. Wei, H. J. Cho, and H. Ohta, *Small* **15**, 1805394 (2019).
- <sup>18</sup>A. V. Sanchela, T. Onozato, B. Feng, Y. Ikuhara, and H. Ohta, *Phys. Rev. Mater.* **1**, 034603 (2017).
- <sup>19</sup>H. Ohta, T. Mizuno, S. J. Zheng, T. Kato, Y. Ikuhara, K. Abe, H. Kumomi, K. Nomura, and H. Hosono, *Adv. Mater.* **24**, 740 (2012).
- <sup>20</sup>H. Ohta, Y. Masuoka, R. Asahi, T. Kato, Y. Ikuhara, K. Nomura, and H. Hosono, *Appl. Phys. Lett.* **95**, 113505 (2009).
- <sup>21</sup>H. Ohta, S. W. Kim, S. Kaneki, A. Yamamoto, and T. Hashizume, *Adv. Sci.* **5**, 1700696 (2018).
- <sup>22</sup>H. Koide, Y. Nagao, K. Koumoto, Y. Takasaki, T. Umemura, T. Kato, Y. Ikuhara, and H. Ohta, *Appl. Phys. Lett.* **97**, 182105 (2010).
- <sup>23</sup>K. Reimann and M. Steube, *Solid State Commun.* **105**, 649 (1998).
- <sup>24</sup>M. B. Sahana, C. Sudakar, A. Dixit, J. S. Thakur, R. Naik, and V. M. Naik, *Acta Mater.* **60**, 1072 (2012).
- <sup>25</sup>Y. Nagao, A. Yoshikawa, K. Koumoto, T. Kato, Y. Ikuhara, and H. Ohta, *Appl. Phys. Lett.* **97**, 172112 (2010).
- <sup>26</sup>K. D. Schierbaum, U. Weimar, W. Gopel, and R. Kowalkowski, *Sens. Actuators, B* **3**, 205 (1991).